eprints@whiterose.ac.uk
https://eprints.whiterose.ac.uk/

1
2
3
4
5
6
7
8
9
10
11
12
13
14
15
16
17
18
19
20
21
22
23
24
25
26
27
28
29
30
31
32
33
34
35
36
37
38
39
40
41
42
43
44
45
46
47
48
49
50
51
52
53
54
55
56
57
58
59
60

Nanostructure and strain properties of core-shell GaAs/AlGaAs nanowires

Th. Kehagias[1], N. Florini[1], J. Kioseoglou[1], Th. Pavloudis[1], Ph. Komninou[1], T. Walther[2], K. Moratis[3], Z. Hatzopoulos[3], N. T. Pelekanos[3]

[1] Physics Department, Aristotle University of Thessaloniki, 54124 Thessaloniki, Greece

[2] Department of Electronic and Electrical Engineering, University of Sheffield, Mappin St, Sheffield S1 3JD, UK

[3] Materials Science & Technology and Physics Departments, University of Crete and IESL/FORTH, GR-71003 Heraklion, Greece

E-mail: kehagias@auth.gr

Abstract

GaAs/AlGaAs core-shell nanowires were grown on Si(111) by Ga-assisted molecular beam epitaxy via the vapor-liquid-solid mechanism. High-resolution and scanning transmission electron microscopy observations showed that nanowires were predominantly zinc-blende single crystals of hexagonal shape, grown along the [111] direction. GaAs core nanowires emerged from the Si surface and subsequently, the nanowire growth front advanced by a continuous sequence of (111) rotational twins, while the AlGaAs shell lattice was perfectly aligned with the core lattice. Occasionally, single or multiple stacking faults induced wurtzite structure nanowire pockets. The AlGaAs shell occupied at least half of the nanowire's projected diameter, while the average Al content of the shell, estimated by energy dispersive X-ray analysis, was x = 0.35. Furthermore, molecular dynamics simulations of hexagonal cross-section nanowire slices, under a new parametrization of the Tersoff interatomic potential for AlAs, showed increased atom relaxation at the hexagon vertices of the shell. This, in conjunction with the compressively strained $Al_{0.35}Ga_{0.65}As$ shell close to the GaAs core, can trigger a kinetic surface mechanism that could drive Al adatoms to accumulate at the relaxed sites of the shell, namely along the diagonals of the shell's hexagon. Moreover, the absence of long-range stresses in the $GaAs/Al_{0.35}Ga_{0.65}As$ core-shell system may account for a highly stable heterostructure. The latter was consolidated by temperature-dependent photoluminescence spectroscopy.

1. Introduction

Semiconductor nanowires (NWs) as one-dimensional (1D) nanostructures have drawn the scientific attention, due to their unique properties that stem from their specific structural characteristics, namely the large surface-to-volume ratio and the capability to fabricate relatively defect-free single-crystalline materials with preferred shape, size and material composition. Since semiconductor NWs exhibit high carrier mobility, they are widely used in advanced technology applications, such as solar cells, sensors, light emitting diodes, and lasers [1, 2, 3].

Although Si has dominated the solar cell technologies, III-V compound semiconductors based solar cells present higher efficiencies, due to their increased light absorption and charge mobility. Moreover, integrating the photovoltaic properties of III-V semiconductors into nanostructures such as NWs, further enhancement of the efficiency, due to quantum confinement, is anticipated. Among III-V semiconductors, the GaAs/AlGaAs heterojunction presents high interest, since the minimal lattice mismatch of GaAs and AlAs (0.13%) results in an almost perfect match of the two lattices. Furthermore, by growing the GaAs/AlGaAs heterostructure in NWs with a core-shell configuration, owing to the vertical heterointerfaces, light absorption is separated from carrier collection pathways and hence, excellent optical quality and longer carrier lifetimes can be achieved [4].

The GaAs/AlGaAs core-shell NWs are mostly synthesized using vapor–liquid–solid (VLS) growth [5], by metalorganic chemical vapor deposition (MOCVD) using Au nanoparticles as catalyst [6, 7], or Ga-assisted molecular beam epitaxy (MBE) on Si(111) [8, 9, 10, 11], or Au-assisted MBE on GaAs(111)B substrate [12]. Previous studies have shown that the GaAs/AlGaAs core-shell NWs grow predominantly as cubic zinc-blende (ZB) single crystals, mainly along the <111> direction, perpendicular to the substrate surface [13, 14]. Occasionally, NW segments of hexagonal wurtzite (WZ) structure have been observed to penetrate the ZB structure, as well. In III-V NWs structural defects, such as rotational twins and stacking faults (SFs) along the growth direction of the NWs are often observed, the latter been responsible for the transition between ZB and WZ structures and vice-versa [14, 15]. High density of these defects in the nanometer scale may induce a variation of the band gap and influence electron transport along the NWs [15]. In addition, oxidation of the AlGaAs shell can be avoided by the superposition of a 5 nm GaAs capping layer over the AlGaAs shell [16], or a phosphide shell as in Makhonin *et al*. [17].

Since the chemical composition the $Al_xGa_{1-x}As$ shell affects the optical properties of the GaAs/AlGaAs heterostructures, their compositional analysis becomes important. An irregular variation of the Al content inside the AlGaAs shell has been observed in single shell and multi-shell GaAs/AlGaAs NWs [7, 8, 9, 18, 19]. In particular, (111) cross-sections of NWs revealed Al-rich bands parallel to the <112> diagonal directions and increased Al concentration from the core to the outer surface [8, 9, 10, 18]. Alternatively, Al-poor AlGaAs quantum dot-like structures at the vertices of these bands in $GaAs/Al_{0.33}Ga_{0.77}As$ multi-shell NWs were reported as well [18, 19].

2

In this work, the nanostructure and the core-shell morphology of GaAs/AlGaAs core-shell NWs, grown by Ga-assisted MBE, were investigated by High-Resolution and Scanning Transmission Electron Microscopy (HRTEM-STEM) techniques. In addition, energy dispersive X-ray (EDX) analysis on all sample geometries was carried out to examine the composition of the AlGaAs shell. The experimentally determined nanostructural data and chemical composition of the NWs were then used as an input to molecular dynamics (MD) simulations. The Tersoff interatomic potential was parametrized to accurately describe the AlAs structure and subsequently, all the required atomistic interactions on the modeling of the GaAs/Al_xGa$_{1-x}$As core-shell NWs. The energetic, strain and stress related characteristics were elucidated, by the implementation of multiple MD simulations on a series of models having various shell-to-NW (S/NW) diameter ratios. A surface kinetic mechanism that triggers the preferential incorporation of Al atoms at the vertices of the hexagonal NWs was established. Finally, the structural stability of the core-shell configuration over a wide range of temperatures derived from MD calculations was examined in terms of temperature-dependent photoluminescence (PL) spectroscopy.

2. Experimental details

The core-shell GaAs/AlGaAs NWs were grown on n-type Si(111) substrates via the Ga-assisted VLS mechanism, in a VG80 MBE system, using an As effusion cell. Prior to GaAs growth, the untreated substrate was annealed *in situ* at ≈730 ^{o}C to form pores in the native SiO_2, which would act as nucleation centers. Subsequently, the growth temperature was ramped down to 620 ^{o}C, and the GaAs core NWs were grown for 20 min, using a Ga flux rate of ≈0.5 ML/s and an As to Ga flux ratio of about 2. Under these conditions, the average diameter and length of the NWs were 75 nm and 2.5 μm, respectively, while their areal density was in the range of 10^8 cm^{-2}. The Ga droplets on the NW tips were then consumed by exposing the sample to As flux for 3 min. For the $Al_{0.3}Ga_{0.7}$As shell, the V to III flux ratio was adjusted to about 4, the growth temperature was kept unchanged, while the growth time was 40 min. In order to protect the shell surface from oxidation, a few nm thick overlayer of GaAs was grown around the NWs.

Samples for TEM and STEM observations were prepared in cross-sectional orientation by the standard sandwich technique, followed by mechanical polishing and Ar$^+$ ion milling in the GATAN PIPS. TEM-HRTEM observations were performed in a JEOL-2011 electron microscope operating at 200 kV (point resolution 0.19 nm, C_s=0.5 mm), while STEM and EDX analysis were performed in a JEOL 2010F electron microscope equipped with an Oxford Instruments Si:Li X-ray detector.

Molecular dynamics (MD) simulations were performed employing the LAMMPS simulator [20], using Tersoff interatomic potential [21, 22, 23] under the III-species environment approach [24].

Finally, in order to detect their optical properties, the NWs were characterized by PL spectroscopy. The samples were mounted in a closed-circuit liquid He cooled cryostat and were excited using the

325 nm beam of a He-Cd laser. The PL emission was analyzed with a nitrogen cooled CCD detector attached to a spectrometer.

3. Results and discussion

3.1 Structural properties of GaAs/AlGaAs core-shell NWs

TEM imaging showed that GaAs/AlGaAs core-shell NWs of hexagonal morphology with {110} sidewalls grow along the [111] direction perpendicular to the Si surface [Figure 1(a)]. However, limited parasitic growth along the equivalent inclined <111> directions was observed as well [Figure 1(b)]. A wide range of NW diameters was observed, with the average projected diameter measured at d = 130±50 nm, which promote the ZB phase [15]. Conversely, the average height cannot be measured with absolute certainty, as the tips of numerous NWs were thinned by the ion milling process. Still, their height, estimated from few intact NWs, was more than 2 μm. As shown in Figure 1(a), despite the strong diffraction contrast of the TEM micrographs, when tilting off the [1$\bar{1}$0] zone axis towards the 200 reflection, it was possible to reveal the core-shell configuration of the GaAs/AlGaAs NWs. The growth conditions followed for the growth of the core-shell NWs resulted in the formation of an interfacial layer of mixed GaAs/AlGaAs crystals, which usually concealed the exact origin of NWs, or even merged with them, as seen in Figs. 1(a) and 1(b). Nevertheless, in thinner areas depleted from this crystal layer, it was evident that NWs nucleated directly from the substrate's surface, just over the native amorphous SiO_2 thin layer (1-5 nm thick) covering the entire Si surface [Figure 1(c)]. Although GaAs NWs nucleation sites presumably stem as a consequence of Ga droplets residing inside pores of the SiO_2 layer that reach the surface of the substrate [25], here original GaAs NWs were observed to emerge from the Si oxide layer, while the presence of pores was not evident, or pores did not penetrate the entire SiO_2 thin layer. This may be attributed to the fact that TEM-HRTEM images are 2D projections of 3D material and depending on the random cut of the cross-sectional samples the amorphous interfacial layer may be projected in front of the NWs' nucleation sites. Yet, epitaxial growth of NWs on amorphous material has been observed in MBE growth of self-catalyzed GaAs NWs [26], and massively in self-assembled III-Nitride NWs on Si(111) and was attributed to the natural tendency of one-dimensional structures to grow along the polar <111> and <0001> crystallographic directions without direct contact with the substrate [27, 28, 29].

The main crystal structure of the NWs, determined by electron diffraction analysis and HRTEM, was the cubic ZB structure. Despite the thin amorphous native oxide on the Si(111) surface, the $[1\bar{1}0]_{NW}/[1\bar{1}0]_{Si}$, $(111)_{NW}/(111)_{Si}$ epitaxial orientation relationship was established among the NWs and the substrate [Figure 2(a)]. Furthermore, near the NW/Si interface rather dense (111) rotational twins of the epitaxial orientation can be observed, as identified by selected area electron diffraction (SAED) patterns [Figure 2(a)]. Occasionally, preliminary GaAs growth can also be realized by inclined {111} twin variants, as depicted in the HRTEM image of Figure 2(b). Hence, it is evident

4

that in the initial stages of GaAs NWs growth a high density of rotational twin defects in all <111> directions are formed, as was also observed in GaAs NWs grown on GaAs(111)B [25]. Subsequently, the GaAs growth front advanced with the formation of multiple (111) twins solely normal to the growth direction throughout the length of the NWs [Figure 2(c)]. Actually, NWs grow with a continuous succession of rotational twins, dense in the beginning of growth and sparse later on, that constitute a twinning superlattice as an essential part of the growth mechanism of ZB phase NWs [15].
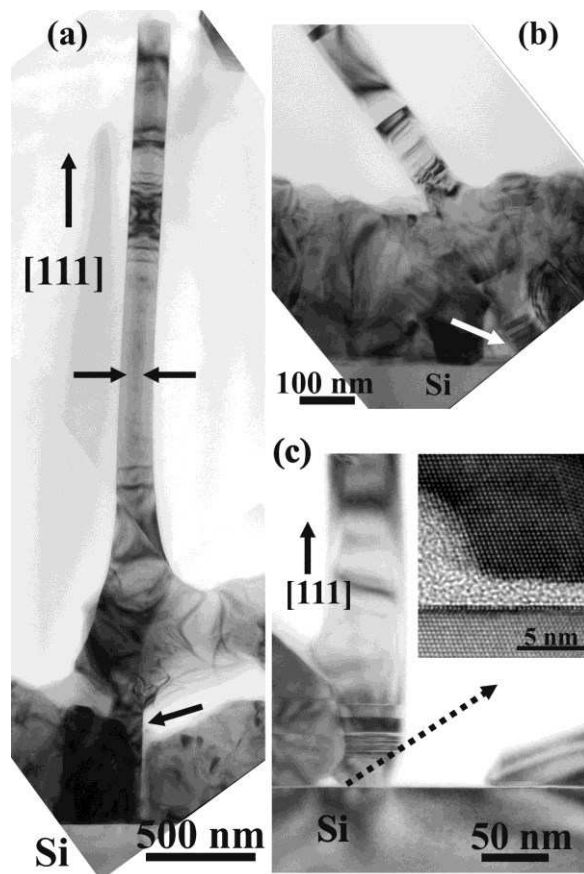

Figure 1. (a) Bright-Field (BF) TEM micrograph, taken off the [1$\bar{1}$0] zone axis, of a GaAs/AlGaAs NW; the core-shell configuration and the original GaAs NW are denoted by arrows. (b) BF TEM micrograph, taken along the [1$\bar{1}$0] zone axis, illustrating an inclined parasitic NW and its origin from the substrate (arrow). (c) Direct nucleation of NWs on the Si surface; the HRTEM image shows that the site of origin is just above the amorphous Si oxide.

There was no evidence that rotational twinning is associated with lattice transformations within the NWs, since the ZB structure was retained on either side of the twin boundaries. Moreover, the presence of the AlGaAs shell did not affect the structural integrity of the GaAs core, as the two lattices were perfectly matched and no structural boundary between the two lattices can be distinguished [Figure 2(c)]. Hence, the structural defects of the core propagated unrestrained in the shell towards the

{110} side facets of the NWs. In the absence of any interfacial dislocations between the two structures, a radial epitaxy of AlGaAs shell on the GaAs core is established and the two lattices are under elastic strain. This phenomenon has also been observed in many other low-misfit III-V NW core/shell systems [30, 31, 32, 33].
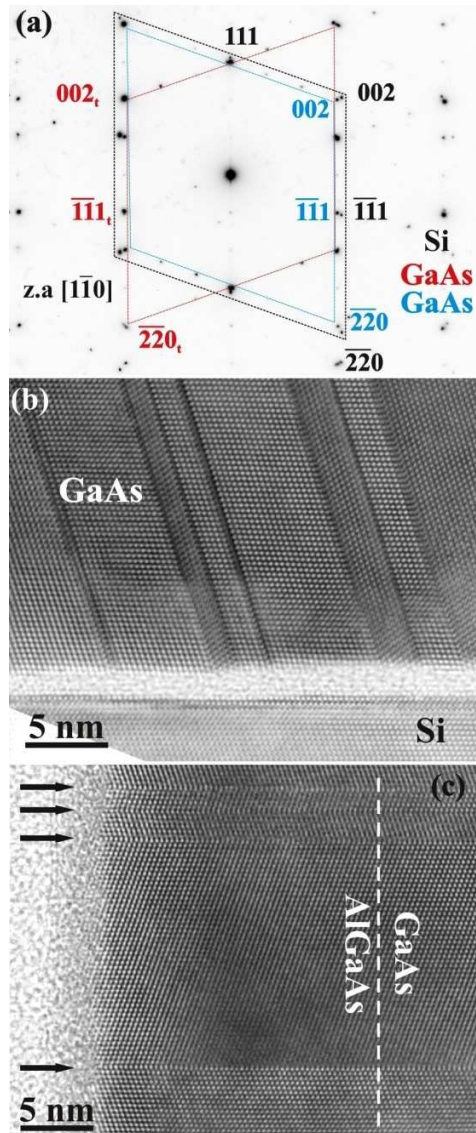

Figure 2 (a) Common SAED pattern of the interfacial area between a NW and Si, in the [1$\bar{1}$0] projection direction, where the epitaxial (blue indices) and its rotational twin (red indices) orientations of GaAs are observed along with Si (black indices). (b) HRTEM image along the [1$\bar{1}$0] zone axis, showing the formation of multiple inclined {111} twins in the initial stages of GaAs growth. (c) HRTEM image of a thin NW viewed along the [1$\bar{1}$0] zone axis, where the continuity between the two lattices is straightforward and the GaAs/AlGaAs boundary is indicative. (111) rotational twin boundaries are denoted by arrows.

Although the GaAs/AlGaAs core-shell NWs grow mainly in the ZB structure, wurtzite (WZ) segments extending from sidewall to sidewall of the NWs were occasionally observed [Figure 3(a)]. The

6

transition between the two structures is achieved either by the insertion of a single or even multiple SFs. Taking the bulk ZB GaAs lattice parameters as reference, we have determined, from HRTEM images, the lattice parameters of the WZ GaAs/AlGaAs structure to be α = 0.395±0.003 nm and c = 0.659±0.003 nm, which are compliant with the values reported from X-ray diffraction analysis [34]. It is apparent that the core-shell structure was not influenced by the lattice transformations [Figure 3(b)]. In the NWs that exhibited WZ segments, these were usually observed near the tips of the NWs mediated between two ZB regions. The formation of WZ pockets persistently near the tips seems to be a consequence of the exposure of the Ga catalyst nanoparticle to the As flux, and can be related to the transfer of the nucleation site from the center of the NW (catalyst droplet) that favors the ZB phase, to the triple phase line that favors the WZ structure [35, 36]. However, in our case, after the extinction of the catalyst particle, further exposure of the NW to the Ga and As beams resulted in a WZ region with thickness that matched the thickness of the underlying ZB structure and the diameter of the NW remained constant. In addition, due to the simultaneous exposure to multiple beams to form the AlGaAs shell, no condensation of a new Ga nanoparticle on the top NW facet was observed [36].
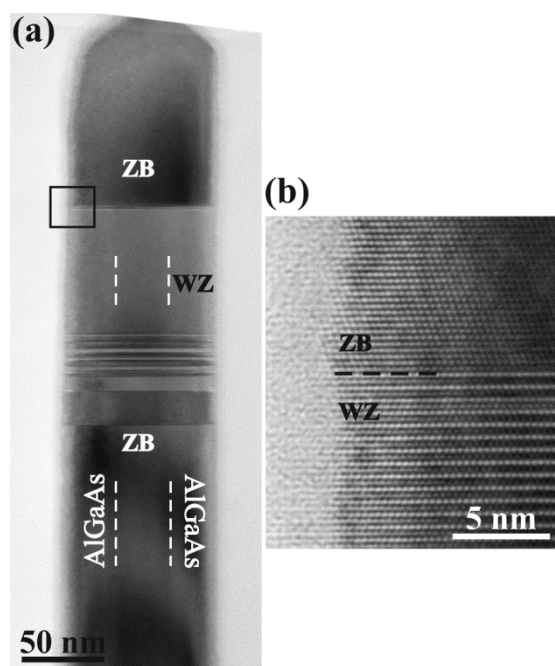

Figure 3 (a) BF TEM micrograph of the top part of a GaAs/AlGaAs core-shell NW, along the [1$\bar{1}$0] zone axis, depicting a segment of WZ structure. (b) HRTEM image of the rectangle area showing the ZB/WZ interface, being a (111) SF.

Furthermore, annular dark-field (ADF) STEM imaging was used to clearly reveal the core-shell structure, and to accurately determine the S/NW projected diameter ratio. As shown in Figure 4(a), the AlGaAs shell extends to one half of the projected diameter of the NW. Taking into account several

measurements, S/NW diameter ratios from 0.45 to 0.65 were determined, the majority being in the range of 0.50-0.55. The average shell thickness of $d_s = 80\pm20$ nm depended on the total thickness of the NW. Moreover, the composition of the $Al_xGa_{1-x}As$ shell was investigated by EDX spectroscopy. The results from cross-sectional EDX line-scans and EDX mapping from planar segments of NWs are shown in Figures 4(b) and 4(c), respectively. In Figure 4(b), the abrupt changes of the Ga content clearly delimit the core boundaries, resulting in a ~90 nm core in a 180 nm thick NW. From Figure 4(c) it is obvious that in the core of the NW there is a clear deficiency of Al and an excess of Ga, while the arsenic concentration remains constant along the diameter of the NW.
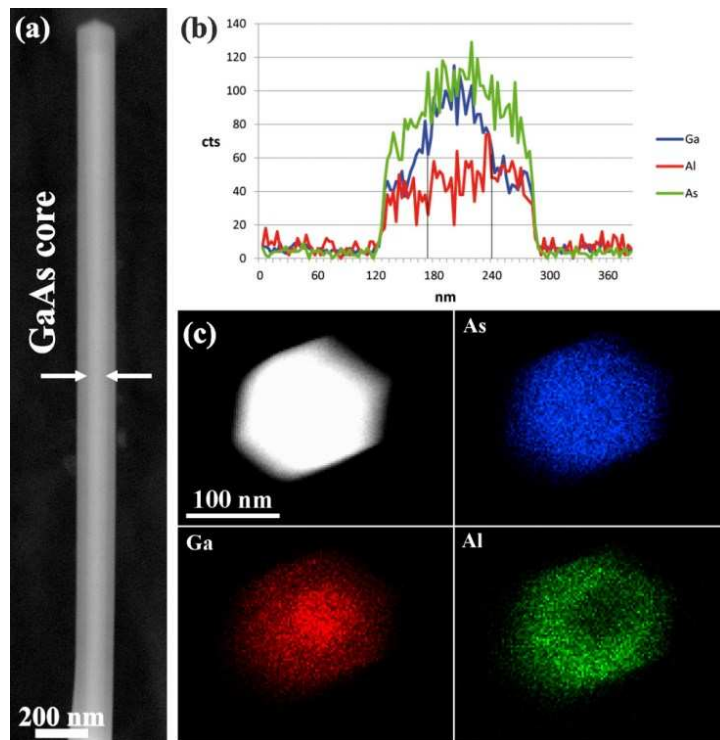

Figure 4 (a) ADF STEM image revealing the GaAs/AlGaAs core-shell structure. (b) Cross-sectional EDX line-scan of the NW in (a), where the boundaries between the core and the shell are discernible. (c) ADF STEM image of a NW's cross-section along with the corresponding EDX elemental maps, showing the distribution of arsenic, gallium and aluminum, respectively.

The EDX data were processed in the Digital Micrograph by summing the K and L maps for Ga and As and multiplying the Al_K map by 2 (as there is no Al_L line map for comparison). Assuming that all k-factors are equal, the Al concentration map was extracted from the following equation [37]:

$$X_{Al} = \frac{2\mathrm{x}Al\ K}{2\mathrm{x}Al\ K + \sum Ga\ K_{\alpha,\beta} + Ga\ L + \sum As\ K_{\alpha,\beta} + As\ L} \quad (1)$$

The calculated atomic concentrations from the Al map varied from 0.20 in the shell to 0.08 inside the core and the calculated atomic concentrations from the Ga map increased from 0.32 from the outer shell to 0.47 inside the core. As these are true atomic concentrations, with scatter by ~ ±0.02, it is necessary to multiply by 2 to get the formula for the group III sub-lattice: the shell will be $Al_{0.4}Ga_{0.6}As$ and the core $Al_{0.06}Ga_{0.94}As$ or pure GaAs, if we assume that the small signal of Al in the core region is probably due to a weak fluorescence effect, and/or a slight tilting of the cross-sectional NW segment from the exact (111) zone axis orientation. If we accept that the core is pure GaAs, then a slight correction of the average Al content of the shell to ~0.35 seems reasonable.

3.2 Molecular dynamics simulations of the NWs

The MD simulations were performed using the Tersoff interatomic potential, hence in order to construct the core-shell atomistic models it was necessary to use the potential parameters of both GaAs and AlAs. The parameters for ZB GaAs potential were derived from [38, 39], while a new full parametrization of the Tersoff interatomic potential was performed for the case of ZB AlAs. In addition, the parametrization of Nordlund *et al.* was used for the Al-Ga interaction [40].

In the Tersoff potential the total energy of a configuration of atoms is given by:

$$E_{coh} = \sum_i \sum_{j \neq i} f_{ij}^c(r_{ij}) \left[V_{ij}^R(r_{ij}) - B_{ij}(r_{ij}) V_{ij}^A(r_{ij}) \right] \quad (2)$$

where i are the atoms, j their neighbors and $r_{ij} = |\mathbf{r}_i - \mathbf{r}_j|$ the pair interatomic distance. B_{ij} is the bond order term of the bond between the atoms i and j, that depends on the neighborhood of both atoms and weakens the attractive pair potential according to its other bonding partners. V_{ij}^R and V_{ij}^A are the pair attractive and repulsive interactions given by Morse potentials as:

$$V_{ij}^R(r_{ij}) = \frac{D_{ij}}{S_{ij} - 1} \exp\left[-\beta_{ij} \sqrt{2S_{ij}} \left(r_{ij} - R_{ij}^0 \right) \right]$$

$$V_{ij}^A(r_{ij}) = \frac{S_{ij} D_{ij}}{S_{ij} - 1} \exp\left[-\beta_{ij} \sqrt{\frac{2}{S_{ij}}} \left(r_{ij} - R_{ij}^0 \right) \right] \quad (3)$$

The bond order terms are:

$$B_{ij}(r_{ij}) = \left\{ 1 + \left[\gamma_{ij} X_{ij}(r_{ij}) \right]^{n_{ij}} \right\}^{-\frac{1}{2n_{ij}}} \quad (4)$$

where X_{ij} is:

$$X_{ij}(r_{ij}) = \sum_{k \neq i, j} f_{ik}^c(r_{ik}) \cdot g_{ik}(\theta_{ijk}) \cdot \exp\left\{ \left[\alpha_{ik} \left(r_{ij} - r_{ik} \right) \right]^{m_{ik}} \right\} \quad (5)$$

9

with θ_{ijk} the angle between r_{ij} and r_{ik}. The angular function that describes the anisotropic interactions is:

$$g_{ik}(\theta_{ijk}) = \delta_{ik}\left[1 + \frac{c_{ik}^2}{d_{ik}^2} - \frac{c_{ik}^2}{d_{ik}^2 + \left(h_{ik} - \cos\theta_{ijk}\right)^2}\right] \quad (6)$$

Finally, the interaction is restricted in a sphere by a cut-off function given by:

$$f_{ij}^c(r_{ij}) = \begin{cases} 1 & r_{ij} - R_{ij}^c \leq -D_{ij}^c \\ \dfrac{1}{2}\left[1 - \sin\left(\pi\dfrac{r_{ij} - R_{ij}^c}{2D_{ij}^c}\right)\right], & \left|r_{ij} - R_{ij}^c\right| < D_{ij}^c \\ 0 & r_{ij} - R_{ij}^c \geq D_{ij}^c \end{cases} \quad (7)$$

The list of the potential parameters used for the ZB AlAs is given in Table 1.

Table 1. The Tersoff interatomic potential parameters used for ZB AlAs [41].

Parameters	AlAs	Parameters	AlAs
R_{ij} (Å)	2.3849	c_{ij}	1.7796
D_{ij} (eV)	2.17	d_{ij}	0.645
B_{ij} (1/Å)	1.5396	h_{ij}	-0.406
S_{ij}	1.1543	n_{ij}	1
γ_{ij}	0.2992	m_{ij}	1
α_{ij}	-1.3824	R_{ij}^c (Å)	3.1
δ_{ij}	0.0424	D_{ij}^c (Å)	0.2

The lattice constants, elastic constants and cohesive energies of the bulk GaAs and AlAs, presented in Table 2, were calculated by the use of the aforementioned interatomic potentials, and were found to agree with the experimental values [42]. The MD simulations were performed under the canonical (NVT) ensemble in 0, 300, 600, 900, 1100 and 1300K, in order to take into account all the temperature depending phenomena and the consequent strain relaxation, close to the growth temperature (~900K). In all cases, the MD simulations were performed on the aforementioned temperatures for 100 ns to ensure that thermal equilibrium is achieved, followed by a rapid quench in order to obtain the energetically favorable ground state configuration.

Table 2. The lattice constant, elastic constants and cohesive energies derived from the LAMMPS calculations for bulk ZB AlAs and GaAs and the corresponding experimental values [42]. B and G are the bulk and the shear moduli, respectively.

	a (Å)	C_{11} (GPa)	C_{12} (GPa)	C_{44} (GPa)	**B** (GPa)	**G** (GPa)	**Cohesive energy** (eV)
AlAs	5.737	140	44	82	76	48	6.88
AlAs *exp.*	5.661	120	57	59	78	32	-
GaAs	5.732	127	39	74	68	44	6.2
GaAs *exp.*	5.653	119	54	59	75	33	-

A series of calculations including full relaxation of the internal degrees of freedom were performed by the use of LAMMPS and the lattice constants and cohesive energies were calculated for the bulk ternary compound $Al_xGa_{1-x}As$ (x = 0-1). The quadratic Vegard's law for the lattice constant and the cohesive energy of the ternary compound is:

$$a = x \cdot a_{AlAs} + (1-x) \cdot a_{GaAs} - b \cdot x \cdot (1-x) \qquad (8)$$

$$E_{coh} = x \cdot E_{coh,AlAs} + (1-x) \cdot E_{coh,GaAs} - b \cdot x \cdot (1-x) \qquad (9)$$

The required fitting procedures were implemented to both data sets and the bowing parameters were extracted. The results shown in Figure 5 suggest that according to our calculations linearity of Vegard's law is valid for the ternary $Al_xGa_{1-x}As$ structure.

In order to elucidate the structural properties of the $GaAs/Al_{0.35}Ga_{0.65}As$ core-shell NWs, a series of atomistic models consisting of 365k-atoms were constructed. According to the experimental observations, their diameter was set at 100 nm and the S/NW ratios ranged from 0.45 to 0.65, for a randomly distributed 0.35 Al content in the shell. Periodic boundary conditions were implemented along the [111] directions, while a vacuum of 10 Å surrounds the NWs, to avoid interactions between the {110} sidewalls. After the structural relaxation, the atom displacements and average stress were calculated by the use of OVITO [43].
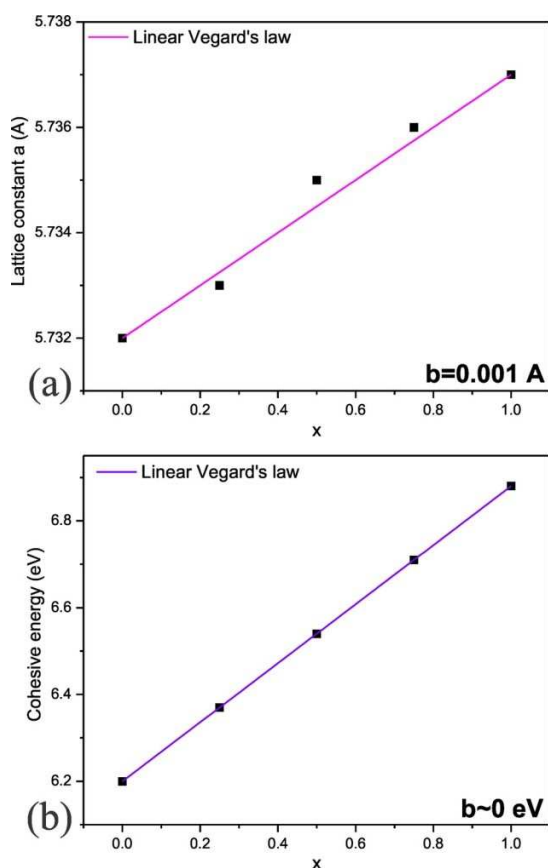
Figure 5 (a) The lattice constant and (b) the cohesive energy of $Al_{0.35}Ga_{0.65}As$ as a function of x. The bowing parameters for both cases are denoted.

The displacement magnitude of each atom after relaxation was calculated with respect to the relaxed positions of the equivalent GaAs NW. Consequently, the displacement value of an atom in a specific radius from the center of the NW is the summation of the displacements of all the atoms closer to the center along this radius. In Figure 6, the displacement magnitude of the atoms of $GaAs/Al_{0.35}Ga_{0.65}As$ core-shell NWs is presented for the various S/NW ratios. The displacement magnitude values of the atomistic models in Figure 6 correspond to the MD simulations for 900K. However, these results did not change over a wide range of examined temperatures (0 to 1300K). The GaAs core atoms did not exhibit significant values of displacements in the smaller S/NW ratios. Only at the core hexagon vertices, the GaAs atoms were displaced with respect to the reference GaAs NW, due to the presence of the $Al_{0.35}Ga_{0.65}As$ shell. The maximum displacement magnitude with respect to the GaAs core was observed at the outer $Al_{0.35}Ga_{0.65}As$ shell hexagon vertices, an area where more degrees of freedom are present for the atoms to relax, and it spreads towards the edges of the outer shell with increasing S/NW ratio, as shown in Figure 6. The $Al_{0.35}Ga_{0.65}As$ atoms on the vertices were found to relax in values close to the bulk $Al_{0.35}Ga_{0.65}As$ lattice constant. On the other hand, the $Al_{0.35}Ga_{0.65}As$ structure was compressively strained close to the core, while it was relaxing towards the outer {110} surfaces. The enhanced relaxation response of the hexagon vertices in conjunction with the compressively strained $Al_{0.35}Ga_{0.65}As$ shell close to the core provides a potential interpretation of the Al-rich paths

along the <112> directions within the $Al_{0.35}Ga_{0.65}As$ shell that were experimentally observed from various groups [8, 9, 10, 18, 44], but not in our experimental setup that did not allow for advanced high-angle ADF observations. This surface kinetic mechanism in the initial stages of the AlGaAs shell radial growth induces an increased incorporation of Al on the relaxed hexagon vertices compared to the compressed {110} facets of the NW. Preferential Al incorporation at the vertices leads to an increased Al concentration along the <112> diagonal directions, and progressively increase the difference on the strain state between the compressed {110} facets of the NW and the relaxed Al-rich vertices. Furthermore, the corresponding atomistic models of the average stresses showed that only local atomic scale stresses were detected regardless of the S/NW ratio. Only in the case of the thicker shell diameter the GaAs core seemed to be under considerable tensile stress. For the majority of NWs (S/NW 0.50, 0.55) long-range stresses are negligible, allowing the formation of a highly stable core-shell structure.
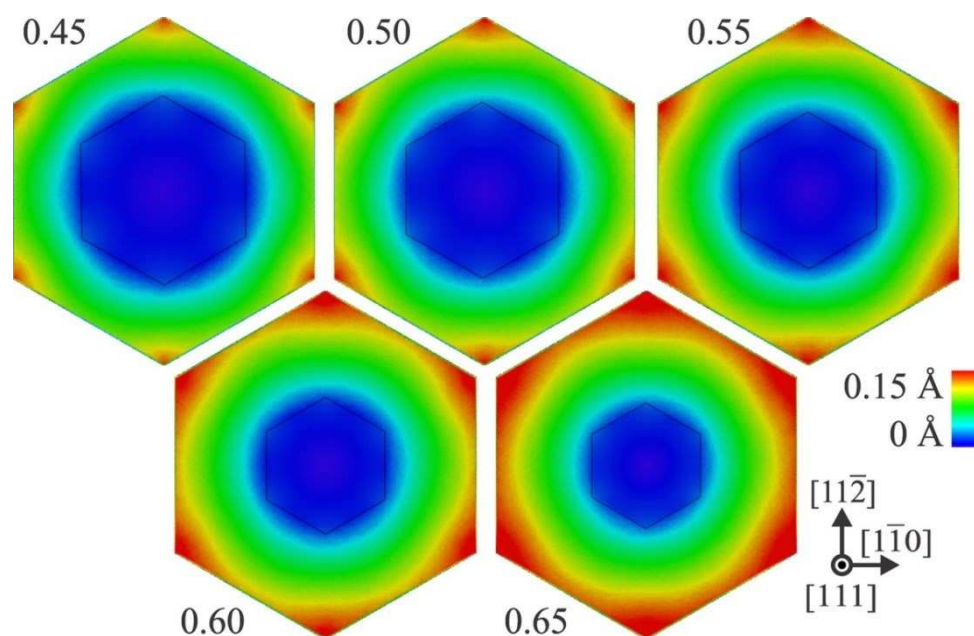
Figure 6 Displacement magnitude of the atoms of $GaAs/Al_{0.35}Ga_{0.65}As$ core/shell NWs. Atoms are pigmented based on the displacement magnitude values following the color bar. The shape of the core is outlined in each case and the corresponding S/NW ratio is also depicted.

In Figure 7, the excess energy per III(Ga or Al)-As pair is calculated versus the S/NW ratio. The excess energy was derived by subtracting the corresponding bulk binding energies for each examined case from the total energy calculated by the MD simulations. While up to 0.50 S/NW ratios the excess energy was almost constant, for higher values the excess energy increased rapidly. This was attributed to the fact that above the 0.50 S/NW ratios the $Al_{0.35}Ga_{0.65}As$ shell induced stress on the GaAs core and consequently, increased the energy level of the GaAs atoms. As shown in the atomistic model of the 0.65 S/NW ratio configuration of Figure 7, the excess energy of the GaAs core atoms is not

negligible. In all cases the atoms of the outer surfaces of the shells were compressed due to surface relaxation phenomena and thus, exhibited higher excess energies.
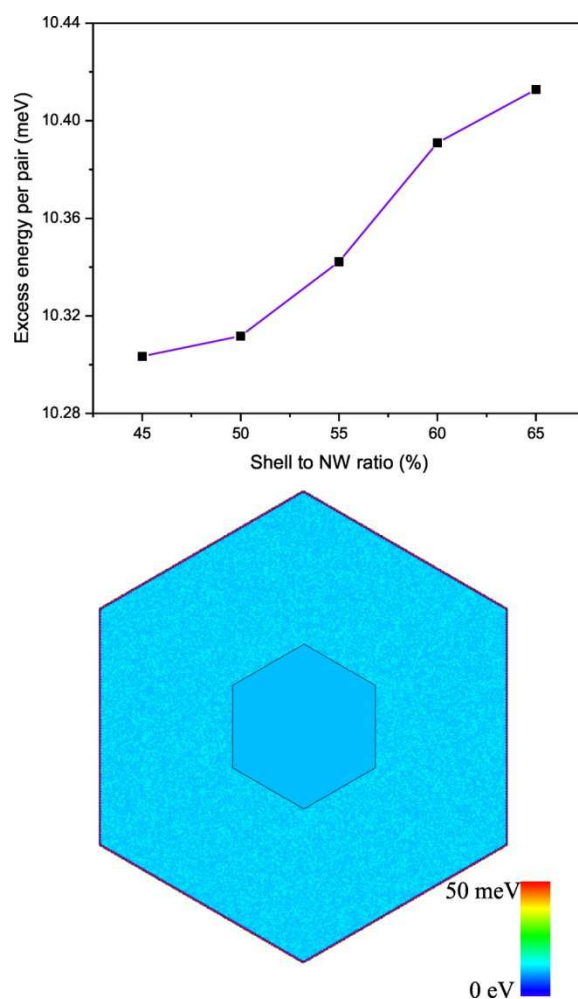

Figure 7 Excess energy per III(Ga or Al)-As pair versus the S/NW ratio. The atomistic model of the 0.65 S/NW ratio configuration. Atoms are pigmented based on the excess energy following the corresponding color bar. The shape of the GaAs core is outlined.

3.3 PL spectroscopy of the NWs

The high structural quality and energetic stability of the $GaAs/Al_xGa_{1-x}As$ (x = 0.3-0.4) core-shell NW configuration detected in TEM observations and MD simulations from 0 to 1300 K is directly reflected in the PL emission of the samples. From temperature dependent macro-PL measurements, obtained from several thousands of NWs, intense PL emission is observed up to elevated temperatures, as depicted in Figure 8(a). The PL emission at wavelengths shorter than 800 nm at 20 K, exhibiting a dominant peak at 790 nm, can be attributed to recombination at localized centers in the AlGaAs shell, such as for instance Al-deficient enclosures, as reported previously by other groups [9, 18]. With increasing temperature, the shorter-wavelength side of the AlGaAs emission loses intensity faster,

while the 790 nm peak persists up to 240 K. An Arrhenius plot of the 790 nm AlGaAs PL peak spectrally-integrated intensity gives a thermal activation energy of ~110 meV, in line with the strongly localized nature of the specific recombination. At low temperatures, the GaAs core PL, occurring in the 820-840 nm range, is dominated by donor-acceptor recombination peaked around 837 nm. With increasing temperature, however, this recombination is rapidly quenched, giving rise to essentially free-exciton (FX) recombination, persisting all the way up to elevated temperatures. The FX GaAs peak position energy at 20 K is 1.505 eV, which is significantly red-shifted with respect to bulk GaAs, as a consequence of residual strain and piezoelectric effects, analyzed elsewhere [44]. In Figure 8(b), we compare the Arrhenius plot of the spectrally-integrated GaAs FX emission for the GaAs/AlGaAs core-shell NWs, with that of a reference sample with bare GaAs NWs, having same structural characteristics as the core part of the core-shell NWs, produced by interrupting the growth just before the shell deposition. First remark is that the FX PL intensity of the core-shell NWs is increased by two orders of magnitude compared to the bare GaAs NWs. This comes as a consequence of efficient passivation of the GaAs surface by the AlGaAs shell, which drastically reduces surface-related non-radiative channels. Second, we observe that while the FX emission of the bare GaAs NWs quenches rapidly above 60K, with a weak activation energy of 35 meV, in the case of the core-shell NWs, the drop in intensity is pushed to about 120K and the corresponding activation energy is increased to 80 meV. Considering the relatively high potential barriers of this NW heterostructure, along with the efficient surface passivation that the AlGaAs shell provides, we interpret the enhanced activation energy for the core PL, to thermal de-trapping of carriers localized in the AlGaAs shell and subsequent transfer to the GaAs core. This interpretation is in line with the similar in magnitude activation energy of the AlGaAs shell PL, mentioned above.
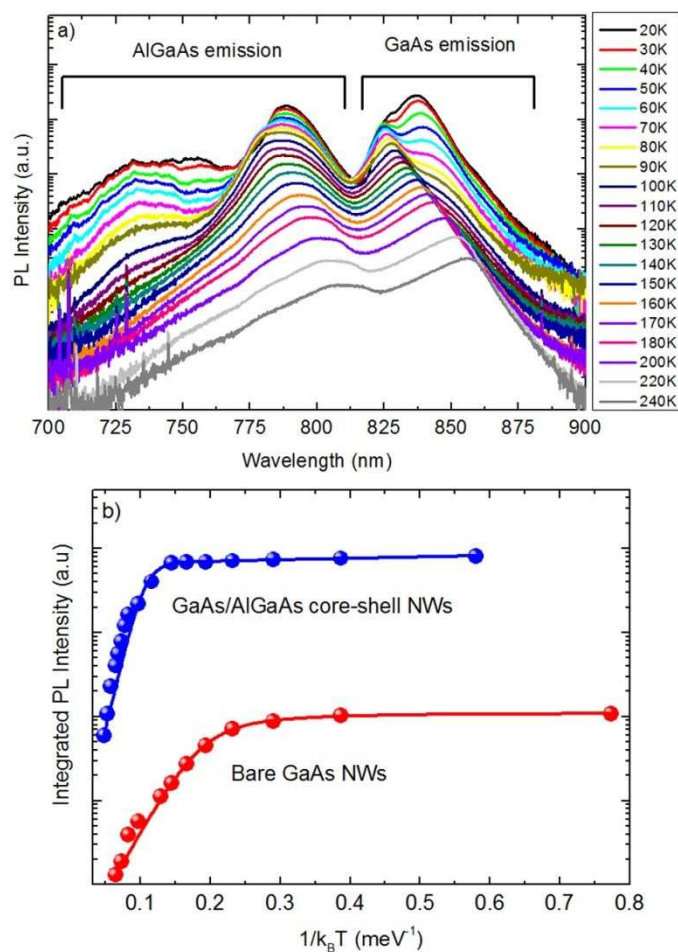
Figure 8 (a) Temperature-dependent PL measurements of ensemble GaAs/AlGaAs core-shell NWs. (b) Arrhenius plots of the spectrally-integrated GaAs FX emission for the GaAs/AlGaAs core-shell NWs and a reference sample with bare GaAs NWs of similar structural characteristics.

4. Conclusions

Predominantly ZB phase single crystalline GaAs/AlGaAs core-shell NWs, grown on Si(111) by MBE, were investigated by HRTEM, STEM, EDX spectroscopy, MD simulations and PL spectroscopy. Core GaAs NWs emerged from the Si surface despite the presence of the amorphous native oxide, along the normal to the surface [111] growth direction. Subsequently, GaAs growth advanced by a (111) rotational twinning superlattice, while growth of the AlGaAs shell was in a perfect epitaxial relationship with the GaAs core. Sporadic WZ segments observed near the tips of the NWs did not influence the core-shell configuration. S/NW diameter ratios of 0.45-0.65 were detected, and an average Al concentration of $x = 0.35$ was determined in the shell. MD simulations, under new parametrization of the Tersoff potential for AlAs, showed maximum atom displacements at the outer vertices of the NW's hexagon and compression of the shell near the core that can account for increased Al concentration paths along the <112> diagonals of the AlGaAs shell. Moreover, the presence of Al in the shell induces only atomic scale stresses, while the excess energies per atom pair

16

1
2
3
4
5
6
7
8
9
10
11
12
13
14
15
16
17
18
19
20
21
22
23
24
25
26
27
28
29
30
31
32
33
34
35
36
37
38
39
40
41
42
43
44
45
46
47
48
49
50
51
52
53
54
55
56
57
58
59
60

are rather low for the majority of NWs with S/NW ratios of 0.50-0.55. These findings, in conjunction with the observed structural integrity of the GaAs/$Al_{0.35}Ga_{0.65}As$ heterostructure, suggest a structurally and energetically stable core-shell configuration over a wide range of temperatures, which was further established by the results of PL measurements showing an effective passivation of the GaAs core from the AlGaAs shell and substantial emission from the NWs from 20 K to 240 K.

Acknowledgements

References

[1] Borgstrom M T, Wallentin J, Heurlin M, Falt St, Wickert P, Leene J, Magnusson M H, Deppert K and Samuelson L 2011 *IEEE J. Sel. Top. Quant.* **17** 1050

[2] Lu W and Lieber Ch M 2006 *J. Phys. D: Appl. Phys.* **39** R387

[3] Dasgupta N P, Sun J S, Liu Ch, Brittman S, Andrews S C, Lim J, Gao H, Yan R and Yang P 2014 *Adv. Mater.* **26** 2137

[4] Lee Y H, Fu L, Li Zh, Breuer St, Parkinson P, Tan H and Jagadish Ch, SPIE, Newsroom, DOI:0.1117/2.1201308.005048

[5] Wagner R S and Ellis W C 1964 *Appl. Phys. Lett.* **4** 89

[6] Fickenscher M, Shi T, Jackson H E, Smith L M, Yarrison-Rice J M, Zheng C, Miller P, Etheridge J, Wong B M, Gao Q, Deshpande S, Tan H H and Jagadish Ch 2013 *Nano Lett.* **13** 1016

[7] Guo J, Huang H, Ding Y, Ji Zh, Liu M, Ren X, Zhang X and Huang Y 2012 *J. Cryst. Growth* **359**, 30

[8] Kauko H, Zheng C L, Zhu Y, Glanvill S, Dwyer C, Munshi A M, Fimland B O, van Helvoort A T J and Etheridge J 2013 *Appl. Phys. Lett.* **103** 232111

[9] Rudolph D, Funk S, Döblinger M, Morkötter S, Hertenberger S, Schweickert L, Becker J, Matich S, Bichler M, Spirkoska D, Zardo I, Finley J J, Abstreiter G, and Koblmüller G 2013 *Nano Lett.* **13** 1522

[10] Munshi A M, Dheeraj D L, Fauske V T, Kim D C, Huh J, Reinertsen J F and Ahtapodov L 2014 *Nano Lett.* **14** 960

[11] Paek J H, Nishiwaki T, Yamaguchi M and Sawaki N 2010 *Physica E* **42** 2722

[12] Zhou H L, Hoang T B, Dheeraj D L, van Helvoort A T J, Liu L, Harmand J C, Fimland B O and Weman H 2009 *Nanotechnology* **20** 415701

[13] Tambe M J, Lim S K, Smith M J, Allard L F and Gradečak S 2008 *Appl. Phys. Lett.* **93** 151917

[14] Tomioka K, Kobayashi Y, Motohisa J, Hara Sh and Fukui T 2009 *Nanotechnology* **20** 145302

[15] Caroff P, Bolinsson J, and Johansson J 2011 *IEEE J. Sel. Top. Quant.* **17** 829

[16] Joyce H J, Gao Q, Tan H H, Jagadish Ch, Kim Y, Zhang X, Guo Y and Zou J 2007 *Nano Lett.* **7** 921

[17] Makhonin M N, Foster A P, Krysa A B, Fry P W, Davies D G, Grange T, Walther T, Skolnick M S, and Wilson L R 2013 *Nano Lett.* **13** 861

[18] Heiss M, Fontana Y, Gustafsson A, Wüst G, Magen C, O'Regan D D, Luo J W, Ketterer B, Conesa-Boj S, Kuhlmann A V, Houel J, Russo-Averchi E, Morante J R, Cantoni M, Marzari N, Arbiol J, Zunger A, Warburton R J and Fontcuberta i Morral A 2013 *Nat. Mater.* **12** 439

[19] Mancini L, Fontana Y, Conesa-Boj S, Blum I, Vurpillot F, Francaviglia L, Russo-Averchi E, Heiss M, Arbiol J, Fontcuberta i Morral A and Rigutti L 2014 *Appl. Phys. Lett.* **105** 243106

[20] Plimpton S 1995 *J. Comput. Phys.* **117** 1

[21] Brenner D W 1989 *Phys. Rev. Lett.* **63** 1022

[22] Tersoff J 1989 *Phys. Rev. B* **39** 5566

[23] Tersoff J 1990 *Phys. Rev. B* **41** 3248

[24] Kioseoglou J, Komninou P and Karakostas T 2008 *Phys. Stat. Sol. B* **245** 1118

[25] Fontcuberta i Morral A, Colombo C, Abstreiter G, Arbiol J, and Morante J R 2008 *Appl. Phys. Lett.* **92** 063112

[26] Rieger T, Luysberg M, Schäpers T, Grützmacher D, and Lepsa M I 2012 *Nano Lett.* **12** 5559

[27] Furtmayr F, Vielemeyer M, Stutzmann M, Arbiol J, Estradé S, Peirò F, Morante J R, and Eickhoff M 2008 *J. Appl. Phys.* **104** 034309

[28] Kehagias Th 2010 *Physica E* **42** 2197

[29] Geelhaar L, Chèze C, Jenichen B, Brandt O, Pfüller C, Münch S, Rothemund R, Reitzenstein S, Forchel A, Kehagias T, Komninou P, Dimitrakopulos G P, Karakostas T, Lari L, Chalker P R, Gass M H, and Riechert H 2011 *IEEE J. Sel. Top. Quant.* **17** 878

[30] Dellas N S, Liang J, Cooley B J, Samarth N, and Mohney S E 2010 *Appl. Phys. Lett.* **97** 072505

[31] Jabeen F, Grillo V, Martelli F, and Rubini S 2011 *IEEE J. Sel. Top. Quant.* **17** 794

[32] Yu X, Wang H, Pan D, Zhao J, Misuraca J, von Molnár S, and Xiong P 2013 *Nano Lett.* **13** 1572

[33] Šiušys A, Sadowski J, Sawicki M, Kret S, Wojciechowski T, Gas K, Szuszkiewicz W, Kaminska A, Story T 2014 *Nano Lett.* **14** 4263

[34] McMahon M I and Nelmes R J 2005 *Phys. Rev. Lett.* **95** 215505

[35] Cirlin G E, Dubrovskii V G, Samsonenko Yu B, Bouravleuv A D, Durose K, Proskuryakov Y Y, Mendes B, Bowen L, Kaliteevski M A, Abram R A, and Zeze D 2010 *Phys. Rev. B* **82** 035302

[36] Priante G, Ambrosini S, Dubrovskii V G, Franciosi A, and Rubini S 2013 *Cryst. Growth Des.* **13** 3976

[37] Walther T, Humphreys C J, Cullis A G and Robbins D J 1995 *Mater. Sci. Forum* **196-201** 505

[38] Hammerschmidt T, Kratzer P and Scheffler M 2008 *Phys. Rev. B* **77** 235303

[39] Hammerschmidt T, Kratzer P and Scheffler M 2010 *Phys. Rev. B* **81** 159905

[40] Nordlund K, Nord J, Frantz J, and Keinonen J 2000 *J. Comput. Mater. Sci.* **18** 283

[41] The interatomic potential file for LAMMPS is available and will be provided upon request

[42] Adachi S 1985 *J. Appl. Phys.* **58** R1

[43] Stukowski A 2010 *Modelling Simul. Mater. Sci. Eng.* **18** 015012 (Software available at http://ovito.org/)

[44] Hocevar M, Thanh Giang L T, Songmuang R, den Hertog M, Besombes L, Bleuse J, Niquet Y M and Pelekanos N T 2013 *Appl. Phys. Lett.* **102** 191103